

Electronic Supplementary Information (ESI) available:

Ultrasensitive Photodetectors Based on High-Quality LiInSe₂ Single Crystal

Ning Jia,^a Shanpeng Wang,^{*, a, b} Pengfei Wang,^c Chunlong Li,^a TongTong Yu,^a Jie Qiao,^a Chenning Li,^a Xixi Xiong,^a Jia-Lin Sun,^c and Xutang Tao^{*, a, b}

^a State Key Laboratory of Crystal Materials, Shandong University, Jinan 250100, China

^b Key Laboratory of Functional Crystal Materials and Device (Shandong University, Ministry of Education), Jinan, 250100, China

^c State Key Laboratory of Low-Dimensional Quantum Physics, Department of Physics, Tsinghua University, Beijing 100084, China

* txt@sdu.edu.cn; wshp@sdu.edu.cn

S1. Polycrystalline synthesis and crystal growth

The polycrystalline of LISe was synthesized by a traditional solid state reaction. Commercial available Li (99.9%), In (99.999%), and Se (99.999%) were purchased from Aladdin Chemical Reagent Co., Ltd. (Shanghai, China) and used after further purification. The raw materials were accurately weighed according to the stoichiometric ratio of LISe with a 0.1% excess of Li and 0.2% of Se. Bulk LISe crystal was grown by a modified Bridgman method using an oriented seed crystal. The synthesized polycrystalline material was loaded in a graphite crucible and then sealed in a quartz ampule under 1×10^{-3} Pa. During the growth of LISe crystal, the following growth parameters were used: temperature gradient 15 °C/cm and growth rate of 1 mm/h. Finally, a large-sized LISe single crystal could be obtained after the furnace was cooled to room temperature at a cooling rate of about 50 °C/h.

A single-phase polycrystalline LISe ingot was obtained. XRD data for polycrystalline LISe in combination with Rietveld refinements allowed the phase purity to be assessed. The powder XRD diffraction patterns are in good agreement with the

calculated diffraction patterns of the single crystal, as shown in Fig. S1. The results of Rietveld refinements yielded excellent discrepancy values, $R_p = 6.86\%$, $R_{wp} = 9.16\%$, indicating that polycrystalline LISe was of high phase purity.

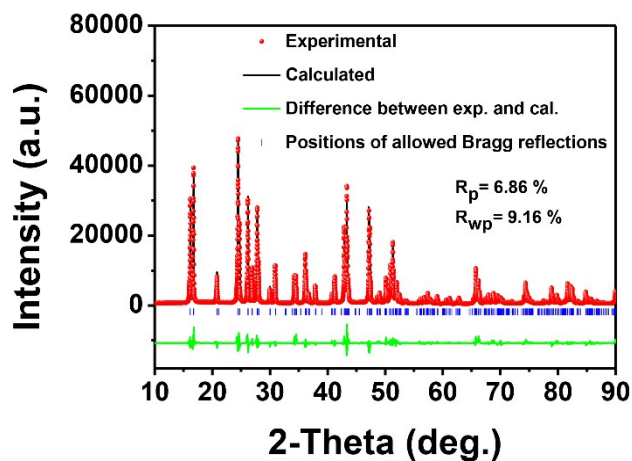


Fig. S1 Rietveld refinement pattern for polycrystalline LISe. Experimental (red dot), calculated (black line), and their difference (green trace). The tick marks (blue) indicate the positions of the allowed Bragg reflections.

S2. Schematic diagram of the Au interdigital electrode sizes

In the photoresponse measurement, Au interdigital electrode was integrated to collect the current, with each electrode consisting of a group of 4 fine Au wires (2.5mm in length, and 0.1mm in width). The schematic diagram of the Au interdigital electrode was shown in Fig. S2. The effective illuminated area was calculated to be 2.5 mm².



Fig. S2 Schematic diagram of Au interdigital electrode.

S3. Optical homogeneity measurement for LISe sample.

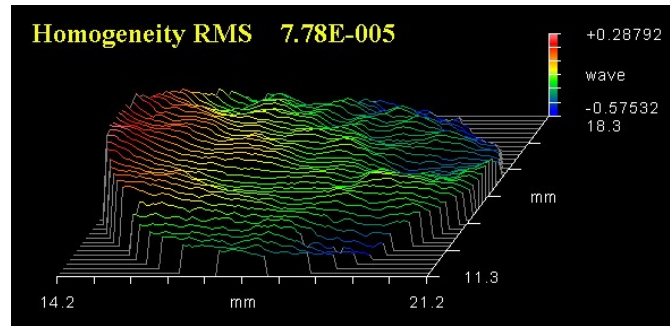


Fig. S3 Optical homogeneity in a realistic fixed 3D view for LISe crystal.

S4. Schematic positions of HRXRD measurements

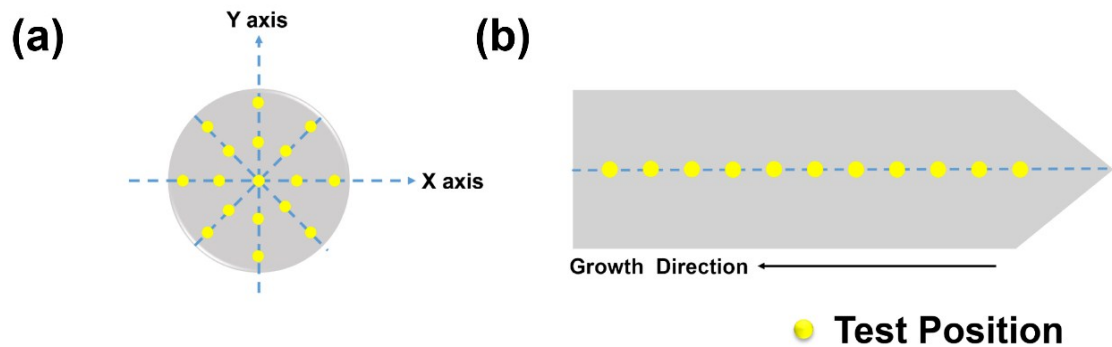


Fig. S4 Schematic positions of HRXRD measurements for (a) perpendicular and (b) parallel to the growth direction.

S5. Working mechanism of the LISe photodetector.

The working mechanism of the LISe based photodetector is illustrated in Fig. S5. The MSM contacts lead to band bending between Au electrodes and LISe. An electrical potential was created when applying an external bias from left electrode to right electrode. Once illuminated with light, the LISe device captures photons largely. Then, the energy absorbed excites electron transition from conductive band to valance band, which generates electron-hole pairs. After that, the electron-hole pairs are separated by the external bias, which turning out to the photocurrent.

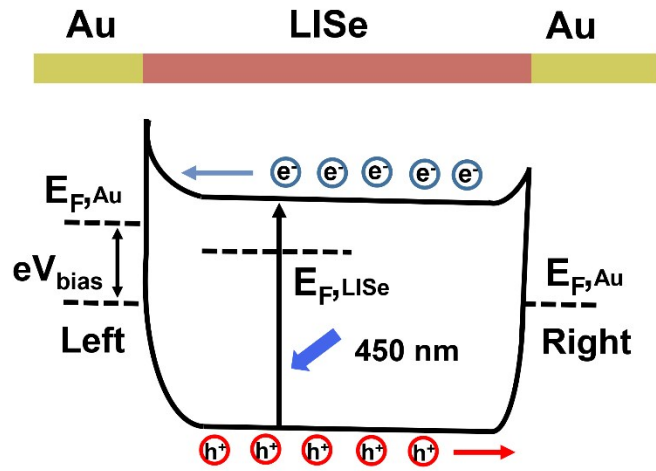


Fig. S5 Working mechanism for LiSe based photodetector.

S6. Room temperature $I - V$ characteristics of both fabricated LiSe-based photodetectors.

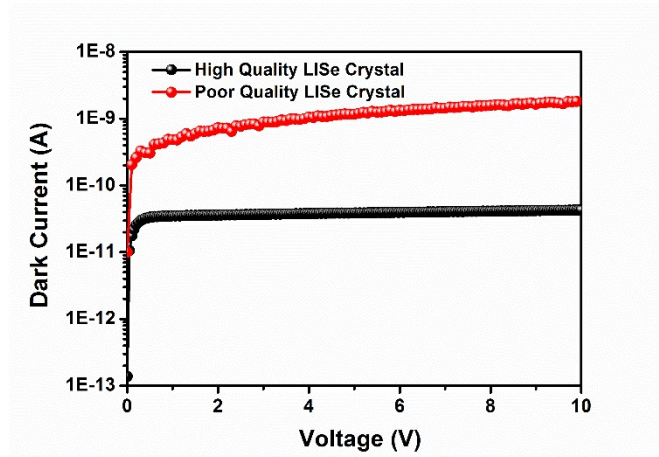


Fig. S6 $I - V$ characteristics of both fabricated LiSe-based photodetectors.

S7. The photocurrent as a function of different illuminate power intensitiy.

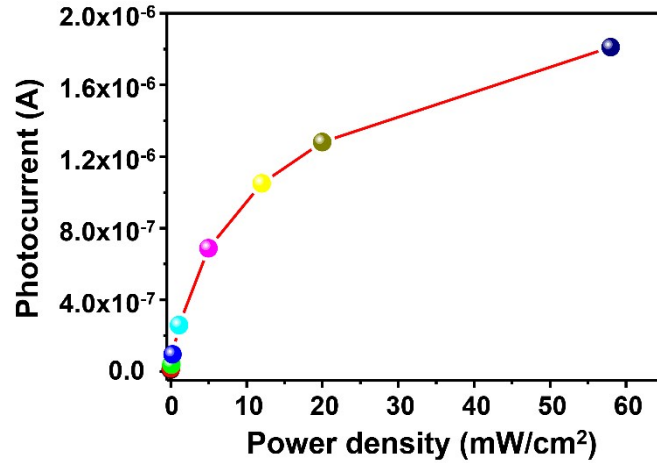


Fig. S7 Dynamic range of LISe based device, i.e., photocurrent vs incident light intensity under 450 nm.

S8. Time dependent photocurrents with irradiation power density of 58 mW/cm² at different applied voltage.

Fig. S8 shows the photo-switching characteristics of the device with irradiation power density of 58 mW/cm² at different applied voltages. The on / off current ratio are 1.23×10^4 , 2.47×10^4 , 3.77×10^4 , 5.17×10^4 and 6.80×10^4 corresponding to the applied voltages of 2, 4, 6, 8, and 10 V, respectively. The on / off current ratios were reproducible without any attenuation for multiple cycles at different applied voltage, showing favorable repeatability and stability of the LISe based photodetector.

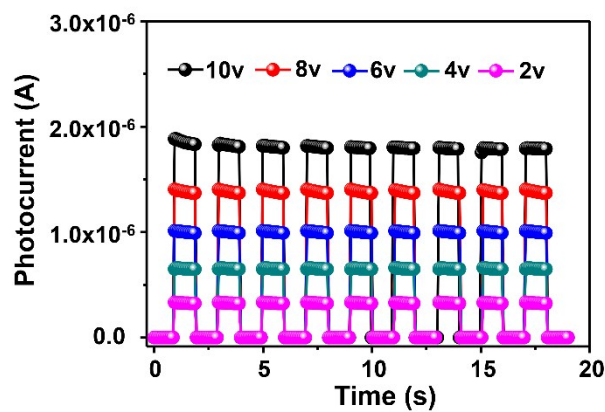


Fig. S8 Time dependent photocurrents with power density of 58 mW/cm² at different

applied voltage.

S9. External quantum efficiency of the LISe based photodetector at different illumination power intensity.

With an irradiation power density of $10 \mu\text{W}/\text{cm}^2$ and 10 V, the highest external quantum efficiency under 450 nm illumination is 10.80%, as shown in Fig. S9.

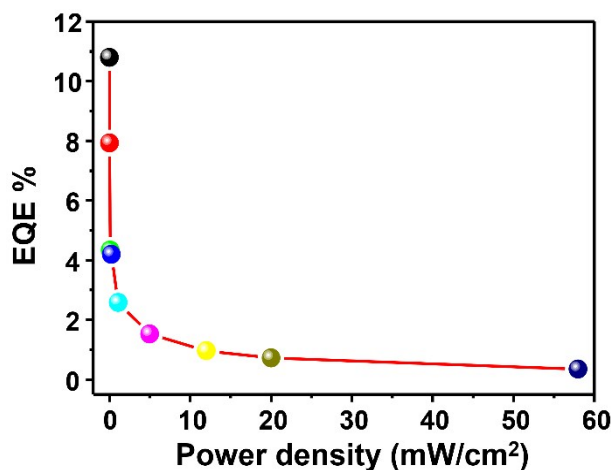


Fig. S9 External quantum efficiency of the LISe based photodetector at different illumination power intensity under 450 nm at 10 V bias.

S10. Photocurrent of the LISe based photodetector at different illumination wavelength under 375 nm, 450 nm, 532 nm, and 633 nm.

The properties of LISe based photodetector at different illumination wavelength under 375 nm, 450 nm, 532 nm, and 633 nm are shown in Fig. S10. Under the same illumination power intensity of $3.2 \text{ mW}/\text{cm}^2$ at a 10 V bias, the photocurrents are $2.11 \times 10^{-7} \text{ A}$, $5.20 \times 10^{-7} \text{ A}$, $2.42 \times 10^{-7} \text{ A}$, and $6.88 \times 10^{-8} \text{ A}$ corresponding to the applied illumination wavelength of 375 nm, 450 nm, 532 nm, and 633 nm, respectively. Summary of important characteristics of the LISe based photodetector under different illumination wavelength are illustrated in Table S1. These results suggest LISe can be harnessed for broadband photodetection from ultraviolet to visible range.

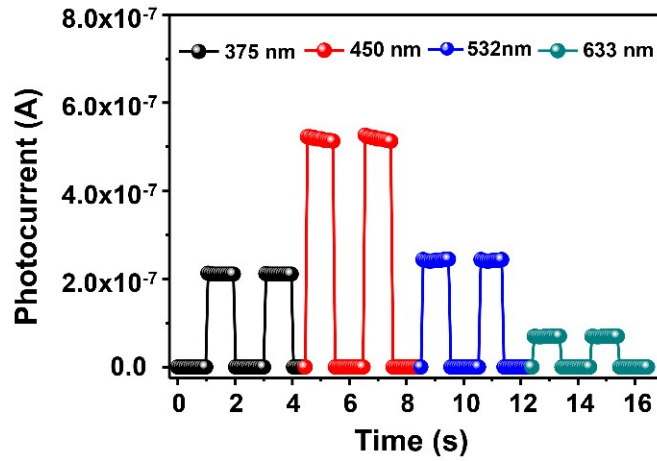


Fig. S10 Photocurrent of LISe-based photodetector at different illumination wavelength under 375 nm, 450 nm, 532 nm, and 633 nm, respectively.

Table S1. Summary of important LISe-based device characteristics under different illumination wavelength.

Wavelength (nm)	On / off current ratio	R (mA/W)	D* (Jones)
375	8.0×10^3	2.63	1.45×10^{11}
450	1.95×10^4	6.54	3.61×10^{11}
532	9.17×10^3	3.03	1.67×10^{11}
633	2.61×10^3	0.85	4.77×10^{10}